ID 82

# Rotor Wake Modelling in Ground Effect Conditions

A. Filippone*, R. Bakker†, P.M. Basset & B. Rodriguez‡,
R. Green§, B. Kutz & F. Bensing¶, A. Visingardi‖

**Abstract**

In this contribution we address the nature of helicopter rotor wakes in presence of the ground. We present some problems of helicopter flight on a flat surface, a validation exercise for a hover in ground effect (Light's experiment) and novel experiments on scaled rotor in advancing flight. We present briefly the computational methods used for this validation exercise. The methods range from lifting line to unsteady Reynolds-averaged Navier-Stokes equations. Validations are shown for out-of-ground and various ground clearances.

## 1 Introduction

The ground effect problem is not a new one. It has been investigated in one form or another for at least fifty years. Although the problem is not amenable to simple aerodynamic solutions, semi-empirical formulas have been developed to quantify the effects of ground proximity on rotor power and thrust, in particular the effects on shaft power at specified thrust and the effects on thrust at specified shaft power. One of the earliest examinations is due to Betz[1]. Better equations include Knight & Hefner[2], Cheeseman & Bennett[3], Hayden[4]. The cited papers aimed at the determination of integral rotor performance, such as power for a specified thrust and thrust for a specified power over a variety of ground clearances. All the experimental data indicate that the ground effect becomes noticeable at about one rotor diameter from the ground and becomes stronger as the rotor approaches the ground. Most experimental data go as close as 1/4 rotor diameter, which is the practical limit of full size helicopters.

Over the years, research has expanded to include several aspects. The research on ground effects is afferent to three distinct strands: 1.) Ground effect, with particular reference to flat and inclined surfaces, with and without the presence of a nearby wall or other obstacle; 2.) Ground effects on unpaved airfields, with particular interest to raising and re-ingestion of sand (*brownout*); 3.) ship-board operations, with reference to large scale effects due to tower and gusts and with respect to shipdeck motion. This contribution focusses on the first strand of research.

As far as the wake itself is concerned, its dynamics affects not only the rotor loads, but also the rotorcraft dynamics, aircraft stability and control and safety of ground personnel, as well as impacts on nearby objects (roofs, vehicles, etc.). Complications arise from all sorts of interactions, beyond the aircraft itself, including the solid surfaces and atmospheric turbulence. The unsteady and re-circulatory nature of the flows that are set up when the wake interacts with the ground and other obstacles plays an important part in defining the envelope within which the rotorcraft is allowed to operate safely. For both military and civil operations, recirculation of sand and snow particles makes hovering close to the ground and landing very difficult. The available flight envelope for operation off the back of ships can be severely constrained by the interaction of the wake from the ship superstructure with the helicopter's own wake under certain wind conditions. During airport/airfield operations, the downwash (and also the "side-wash", as the wake moves outwards, parallel to the ground) that is induced when hover-taxiing must be considered when manoeuvring near other aircraft and buildings.

The key flight parameters affecting the wake shape

*The University of Manchester, United Kingdom; Corresponding author: E-mail: a.filippone@manchester.ac.uk
†NLR, Amsterdam, NL
‡ONERA, The French Aerospace Lab, Salon de Provence, France
§University of Glasgow, School of Eng., United Kingdom
¶University of Stuttgart, IAG, Germany
‖CIRA, Capua, Italy

and the rotor performance on solid ground are the height of the rotor blade with respect to the ground (*clearance*), the forward speed $V_\infty$, the rotor inclination $\alpha$, and the thrust coefficient $C_T$. These parameters are used to define the *thrust-weighted advance-ratio* $\mu^* = \mu/\sqrt{C_T/2}$ where $\mu$ is the conventional advance ratio of a helicopter rotor, $\mu = V_\infty \cos\alpha/\Omega R$. Different wake regimes[5] are identified, depending on the value of $\mu*$.

The experimental work by McCauley et al.[6] addressed helicopter rotors in ground effect above horizontal and inclined surfaces. The latter case is relevant to cases of ground manouevres and tactical engagement. Since the rotor tips come closer to the ground as they reach the forward position, the problem is compounded by additional unsteady aero-mechanics problems, including stronger variation of the aerodynamic coefficients and enhanced flapping.

One case of unprepared airfields is of special concern in helicopter operations: sandy desert. Upon landing, take-off and ground manoeuvre, the rotor downwash can raise a large dust cloud that limits visibility and is a serious flight safety risk. This problem is called *brownout*. Furthermore, dust recirculating around the aircraft can cause considerable damage to the turboshaft engines, as ingestion of particulate is almost inevitable[7].

The GARTEUR Action Group HC-AG17 was launched to address all these wake-related problems. This paper presents some results obtained by the working group.

## 2 Computational Methods

A number of aerodynamic models exist for the simulation of helicopter wakes. We will discuss the models used for this study in order of increasing physical complexity. Most of the models require special conditions in order to calculate the effects of solid fixed and moving ground; unprepared surfaces require additional transport models for the particulate to describe the pick up of the particulate, its dynamics whilst in the air and its interaction with the aircraft surfaces.

### 2.1 Lifting Line and Lifting Surface

This is class of reduced-order methods. Key simplifications include the elimination of blade thickness effects and the assumption of inviscid flow. A number of models have been used for this exercise, and are briefly discussed here.

For the time (manoeuvring) simulations of rotorcraft flight dynamics within the ground effect several approaches have been developed, mainly based on extensions of the Finite State Unsteady Wake model FiSuW[8].

For the purposes of comparisons with the positions of the blade tip vortices of a hovering rotor, another approach has been applied. Since the code FiSuW is based on the acceleration potential, there is no actual representation of the rotor wake vortices. Therefore, a vortex wake approach called SilAnx has been used for these comparisons.

**Lifting Line Code SilAnx.** The SilAnx model is a vortex wake model made of groups of multi-circular vortices. The geometry of the rotor wake is presented in Fig. 1. The idea behind its creation was to get a rotor vortex wake model simple enough in its geometry to require a low computational time for flight dynamics simulations. Thus, simple vortex shapes are used: circular vortices for the trailing vortices and rectilinear segments for the shed vortices. A new group of concentric vortex rings is emitted at each rotor revolution (the furthest one at the end of the wake downstream is then discarded).

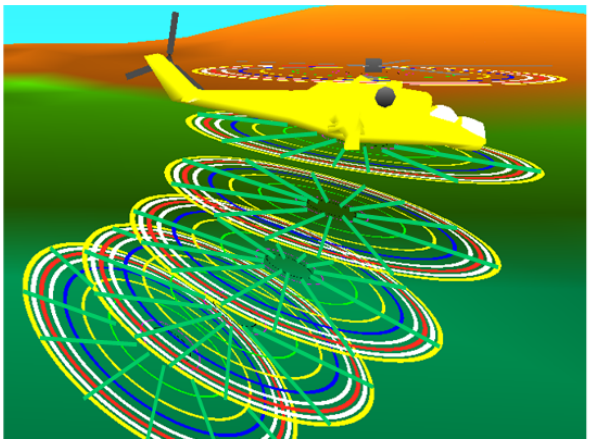

Figure 1: SilAnx rotor wake geometry. For the sake of clarity not all the groups of vortex rings are represented.

The method has been presented in details in Ref.[9]. The method was initially developed for calculating the induced velocities by the main rotor wake on the tail components (horizontal and vertical stabilisers, tail rotor). The induced velocities on the main rotor itself can be calculated by another rotor inflow model or by the SilAnx model itself with a relaxation

method.

In HOGE (hover out of ground effect) the increase of the induced velocities downstream the rotor has for corollary the radial contraction of the rotor wake vein. As well, in HIGE (hover in ground effect) the decrease of the induced velocities normal to the ground leads to a radial expansion of the rotor wake. All that relies on the same first principle: the mass flow rate conservation. At the ground level, the airspeed normal to the ground being null, that implies the expansion of the rotor wake toward an infinite surface on the ground.

By this principle of mass flow rate conservation, the axial (vertical) rotor inflow velocity within the wake and its radial contraction/expansion are in close relationship. Hence the practical extension to the ground effect of the SilAnx model has been implemented through these two aspects. Depending on the height of the rotor above the ground, an altered rotor wake geometry is calculated:

1. The axial distribution of the groups of vortex rings
2. The radial contraction/expansion of the rotor wake.

1) The axial convection velocity of each group of vortex rings is calculated through an iterative process in function of its axial position. If the height with respect to the ground of the considered group of vortices is below one rotor diameter, a transition law between the two following limit conditions is applied: at the rotor level the axial convection velocity in HIGE is the mean induced velocity by the altered wake geometry and at the ground level the axial convection velocity is null. Otherwise, above one rotor diameter with respect to the ground, the position of the vortices is assumed not to be altered by the ground. From this axial velocity, the axial position of the next group of vortex rings is calculated. If this position is below the ground level, it is considered that the group of vortices travels a distance above the ground equal to the one calculated below (rebound-ricochet principle).

2) Out of Ground Effect the ratio of radial variation of vortex rings is calculated with respect to their wake azimuth age with a classical Landgrebe's or Kocurek's law. In Ground Effect this ratio of radial variation is altered by applying a mass flow rate conservation factor:

$$\frac{R_o}{R_{iAge}}_{IGE} = \frac{R_o}{R_{iAge}}_{OGE} \sqrt{\frac{Vim_o}{Viz(iAge)}} \qquad (1)$$

That is the ratio between the initial radius of each ring at the time of its emission by the rotor (depending on the radial discretization in blade elements) and the altered (contracted or expanded) radius at the age given by the index $iAge$. $Vim_0$ is the mean induced velocity at the rotor level, $Viz(iAge)$ is the axial velocity of the group of vortex rings of wake azimuth age $iAge$.

**Free Wake Code MINT.** Lifting line method could also be coupled with free wake model such as the unsteady wake model MINT[10]. This wake model is based on the Mudry theory rigorously describing the unsteady evolution of a wake modelled by a potential discontinuity surface. The wake is discretised with a high order panel representation that allows an accurate wake modelization. It has been coupled with the comprehensive dynamic code HOST[11] which provides the lifting line model and the rotorcraft dynamics. This coupling allows the computation of manoeuvring flights which need an accurate simulation of the wake[12]. In this wake model, the simulation of a flat ground is currently realised by a method of image.

**FlightLab Free Wake Model.** The FlightLab free vortex wake model is based on the Scully model[13], extended with ground effect by introducing a mirror image of the vortex system. The system is build up of an inboard vortex system and tip vortex line segments.

To achieve real-time running of the vortex system the rotor wake is simplified in a few respects. Three basically different wake structures are defined; the near wake, the roll up wake and the far wake. The near wake is the most detailed wake setup. It stretches to an azimuthal wake age of $\pi/N$ ($N$ = number of blades). It consists of shed and trailed vortex lines or sheets. There are as just as many trailed lines as the number of aerodynamic segments of the blade. The number of shed wakes is determined by the increment of the azimuth step. The roll up wake is constructed by an elementary setup of 0 vortex strength at the root, a $\Gamma_{max}$ at a set radial station (input variable) and a $f\Gamma_{max}$ at the blade tip. The roll up wake is supposed to end before the next blade passage. It is meant as an intermediate form between the near and far wake modelling. A far wake system with vortex strength 0 at the root and $\Gamma_{max}$ at the tip is assumed at a wake age of more then $2\pi/N$.

Special care has to be taken for the IGE cases.

The tip vortex is unstable near the ground due to the close distance to the mirror image. Furthermore it is assumed that the inboard wake will diffuse close to ground due to the viscous boundary layer. Based on a mass conservation a set of equations for the radial out flow close to the ground is set up to describe the off set of the tip vortex. A radial outflow regime is assumed at a ground clearance of 0.25R. The tip vortex will follow this ground clearance. The IGE model also requires some parameters to be adapted. The number of revolutions should be increased due to the close spacing of the tip vortices, and the number of iterations should also be increased. The damping has to be decreased.

## 2.2 Boundary Element Method

Boundary element methods are one step up from the lifting surface methods. They include all the thickness effects and are capable of modelling bodies other than lifting surfaces. As such, they can be programmed to simulate aircraft bodies, wing-body combination and even rotorcraft in full configuration. These methods are well-established and have undergone at least thirty years of continuous development and more sophisticated numerical implementations.

The code used in this study is an incompressible, unsteady BEM solver for multi-body, interactional configurations based on Morino's boundary integral formulation[14]. The program solves the Laplace equation for the potential flow in a domain enclosed by the body surface, the wake surface and the far field surface. A sum of source and doublet distributions is placed on the body whereas a vortex layer, fully equivalent to a doublet layer, is placed on the wake. The potential on the body is evaluated by using the Green function method through which an integral expression of Laplace's equation is obtained. The numerical solution of the integral equation is obtained by discretizing the body and wake surfaces by hyperboloidal quadrilateral panels on which the unknown potential is supposed to be constant (zero-th order). The solution of the resulting linear system is obtained by the application of a conjugate gradient method (GMRES solver).

The use of a vortex layer allows the direct application of the Biot-Savart law to calculate the wake-induced velocities. Since the vortex solution becomes singular when the velocity is computed on the vortex itself, the Vatistas equation, accounting for the presence of a core which removes the singularity, is used to evaluate the tangential velocity component induced by each vortex segment:

$$V_\theta(\rho) = \frac{\Gamma\rho}{2\pi(\rho^{2n} + \rho_c^{2n})^{1/n}} \tag{2}$$

where $rho$ is the air density and $\Gamma$ is the circulation. As the exponent $n \to \infty$ the vortex model is reduced to the Rankine vortex; $n = 2$ yields the Lamb-Oseen vortex and $n = 1$ corresponds to the Scully vortex model.

The third-order accurate Adams-Bashfort-Moulton predictor-corrector scheme was used for the update of the wake geometry:

$$\frac{d\mathbf{x}}{dt} = \boldsymbol{v}_i[\mathbf{x}(t),\, t] \tag{3}$$

in which the induced velocity vector $\boldsymbol{v}_i[\mathbf{x}(t),\, t]$ is obtained by application of the Biot-Savart law.

In ground effect operation the wake system distorts and expands under the influence of the ground. This occurrence causes the wake vortex filaments to stretch or shrink, thus producing a corresponding increase or reduction in the swirl velocity surrounding the vortex filament. For these reasons, a modification in the vortex core radius was introduced according to the model proposed by Leishman *et al.*[15].

An efficient Method of Images (MIM) was initially implemented for those conditions in which a symmetry plane could be identified. In the application of the MIM method a great simplification can be obtained by considering that for plane of symmetry and/or ground plane problems the contribution to a generic influence coefficient from mirror image panels, having the same singularity strength as the real panel, is evaluated simply by repeating the calculation for the real panel influencing the mirror images of the control point $\boldsymbol{J}$. This is possible because for incompressible flows the geometrical relationship between the image of a panel $\boldsymbol{I}$ and the point $\boldsymbol{J}$ is identical to that of the real panel $\boldsymbol{I}$ and the image point $\boldsymbol{J}$. This procedure is also more efficient, because it halves the number of unknowns and requires the computations of only the vortices of a half-configuration.

The application of the MIM method, despite accurate and efficient, is only possible when symmetry conditions in the flow field can be detected. This is not the case of a rotor flying in proximity of obstacles of arbitrary shapes and therefore this method cannot be applied. A solution to this problem is represented by the Surface Singularity Method (SSM) which is a more computationally elaborate method but may be applied with greater flexibility. In this approach

the surface of the obstacle is discretised into quadrilateral panels on which a singularity is placed. The strengths associated with each panel are evaluated uniquely subject to the boundary condition of flow tangency at all control points on the surface.

### 2.3 Navier-Stokes Methods

The study shown in this paper was carried out with a version of the FLOWer code[16], which is widely documented in the technical literature. Discretization is realised following the method of lines, where in space second order accuracy is obtained via central differencing stabilised by artificial dissipation operators of second and fourth order according to Jameson[17]. Temporal discretisation can be done by means of local time stepping in case of steady state or dual time stepping[18] for unsteady flow scenarios. When discretizing the Reynolds Averaged Navier Stokes equations, closure of the equations can be provided by one of several available algebraic, one-, two-equation or Reynolds Stress Models. In our case, the standard $k-\omega$ model according to Wilcox[19] is used. The Chimera technique of overlapping grids enables more flexibility concerning grid generation and/or relative motion between different grid components. An Arbitrary Lagrangian Eulerian (ALE) formulation, where motions of the grid nodes due to deformation or rigid body displacements are incorporated into the flux balance, together with a discretization of a Geometric Conservation Law (GCL), which ensures a consistent temporal evolution of deforming control volumes according to their face movements, completes the codes capabilities for helicopter rotor flow simulations.

The vortex transport model (VTM) is a finite volume computational model of the Navier-Stokes equations in vorticity formulation[20;21;22]. The relationship between velocity and vorticity is given by the Biot-Savart equation. The equations are solved with a time-marching scheme on a structured computational mesh. This method has been successfully coupled with a particle transport equation for the simulation of helicopter brownout clouds over a range of helicopter configurations, rotor loads and advance ratios.

## 3 Test Cases

The test cases used for the validation and verification of the aerodynamic models discussed earlier are based on a set of well-defined test data, some of which have been extracted from the existing technical literature, and others have been prepared specifically for this excercise. For the former case, we have chosen the tail rotor experiment by Light[23] (discussed next); for the latter case, we have carried out an experimental campaign that still needs to address the computational validation.

### 3.1 Light's Experimental Data

This test campaign dealt with a hovering rotor set at different heights from the ground and was conducted at the Outdoor Aerodynamic Research Facility at NASA AMES Research Center. The test apparatus consisted of the four-bladed full-scale Lynx tail rotor mounted on the Tail Rotor Test Rig (TRTR). The rectangular blades had a single airfoil NPL9615, no twist and a radius of 1.105 m.

A summary of computer models used for this validation exercise is given in Table 1. In all cases, Fig. 2 to Fig. 6, the top graphs show the axial position of the blade tip vortex during the blade revolution; the bottom graphs show the radial position of the vortex core. The parameters of the analysis include the effective blade loading coefficient $C_T/\sigma$ and the height of the rotor with respect to the ground.

The validation has been performed by evaluating the non-dimensional axial and radial location of the blade tip vortex for five cases selected from those tested during the experimental campaign. Table 2 illustrates the nominal conditions of these cases in terms of blade loading ($C_T/\sigma$); non-dimensional rotor height from the ground ($z/R$); collective pitch ($\theta_o$).

In relation to these conditions, the numerical computations were performed by the following different strategies.

Indeed, the BEM+FW and the MB+FM computations were performed by first trimming the rotor in order to obtain the nominal blade loading, thus allowing a different estimation of the collective pitch; conversely, the URANS and the VTM computations relied on the nominal collective pitch angles, thus allowing a different estimation of the blade loading. The same approach was followed for FD+VRW and LL+FW: trim of the rotor to get the same thrust as in the experiments, which imply differences on the collective.

**HOGE Results.** The analyses of the numerical computations for the tip vortex axial location in

Table 1: *List of computer models used in the validation exercise.*

| Model | Description | Code |
|---|---|---|
| URANS | Unsteady Reynolds-Averaged Navier-Stokes | FLOWer |
| BEM+FW | Boundary Element Method & Free Wake | RAMSYS |
| MB+FM | Multi-body & Flight Mechanics | FlightLab |
| VTM | Vorticity Transport Method | VTM |
| LL+FW | Lifting Line & Free Wake | HOST/MINT |
| FD+VRW | Flight Dynamics & Vortex Ring Wake | HOST/SilAnx |

Table 2: Nominal test conditions.

| $C_T/\sigma$ | $z/R$ | $\theta_o$[deg] |
|---|---|---|
| 0.091 | OGE | 17 |
| 0.080 | 1.54 | 15 |
| 0.071 | 0.84 | 13 |
| 0.090 | 0.52 | 15 |
| 0.095 | 0.52 | 13 |

HOGE conditions, Figure 2a, show a different degree of estimation of the inflow. The MB+FM and LL+VRW methods indicate a general under prediction which results in a tip vortex closer to the rotor disk than the measured one. Conversely, the URANS computation[24] shows the opposite behaviour. VTM computations locate the tip vortex in a position slighter higher than the effective one. The BEM+FW and LL+FW results fall in the range of the experimental results on average. The evaluation of the tip vortex radial location for this flight condition, Figure 2b, shows a global contraction of the wake which is however differently estimated by the computational methodologies: the MB+FM method predicts a linear law for the contraction whereas all the other methodologies are able to reproduce the experimental behaviour in the first 180 degrees. After this azimuth, the VTM shows some scattering in the prediction, and the FD+VRW computations fall generally fall within the range of the experimental measurements. The remaining methodologies all show a tendency to slightly over estimate the wake contraction. Finally, a significant scattering can be observed in the experimental results from the azimuth angle of 200 degrees onward and no qualitative numerical-experimental comparison can therefore be made.

**HIGE Results.** Figures 3 show the location of the tip vortex when the rotor starts operating in HIGE condition, at $z/R = 1.54$. The same considerations made for the axial location in HOGE conditions also hold in this case with the only exception of the MB+FM results which now show a better agreement with the experiment, Fig 3a. The analyses of the radial location, Fig. 3b, show some considerable changes with respect to the HOGE condition and this is mainly due by the effect that the ground starts to exert on the rotor. Both the measurements and the majority of the numerical predictions show an initial wake contraction which is followed by an expansion as soon as the wake approaches the ground. The URANS computations indicate a ground influence much stronger than the actual one (full convergence was not reached); conversely, both the LL+FW and the FD+VRW methods are still marginally sensitive to the ground effect; the BEM+FW calculations reproduce the average experimental behaviour. Finally, the MB+FM methodology evaluates a monotonic contraction which is even stronger than that observed in HOGE conditions.

The tip vortex location in HIGE conditions at $z/R = 0.84$ is shown in the Fig. 4. The axial location clearly indicates a stronger influence of the ground since the tip vortex location is pushed upstream, Fig. 4a. This ground effect is taken into account in the MB+FM method by switching the computation from one wake model to another according to the ground clearance criterion at 0.25R — This approach provides a higher inflow prediction up to the azimuth angle of 300 degrees. The VTM and the FD+VRW computations show a tendency to slight under predict the inflow. The same comment can be made for the BEM+FW methodology but in this case it is likely that it is due by an evaluation of the ground effect which is stronger than the actual one. Both URANS and LL+FW computations slightly over estimate the inflow but the behaviour at azimuth angles higher than 300 degrees is in a reasonable agreement with the experiment. The analysis of the radial location, Fig. 5b shows a significant scattering in the experimental result. In three cases, LL+FW, VTM and FD+VRW, the numerical

predictions are located on the upper boundary of the experimental measurements until the azimuth angle of 300 degrees, whereas the URANS and BEM+FW results generally fall within the range of the measurements. The MB+FM method finally shows a weak wake contraction up to the azimuth of the wake model switch after which it over estimates the ground effect-induced wake expansion.

The analysis of the tip vortex location in HIGE conditions at $z/R = 0.52$ are shown in Fig. 5. The discrepancies in the axial location evaluation, between the numerical predictions and the experimental measurements, Fig. 5a, are much more contained with respect to the previous HIGE conditions. Furthermore, a satisfactory agreement with the measurements can be particularly observed for the URANS and LL+FW computations but also for the FD+VRW results. The VTM calculations predict a slight smaller inflow up to the azimuth angle of 240 degrees after which a sort of plateau is reached and the discrepancy with the measurements increases. The BEM+FW computations are satisfactory for the first 180 degrees after which the behaviour resembles the VTM results. The MB+FM results show a qualitative behaviour similar to the one observed for the previous HIGE condition. The switch in the wake modelling can be observed at about 100 degrees and soon after this azimuth angle the inflow reaches the same value as that evaluated by the VTM and BEM+FW computations at the higher azimuth angles. The evaluation of the radial location, Figure 5b, shows that the VTM predictions are placed along the upper boundary of the experimental results whereas the BEM+FW results are placed along their lower boundary. The URANS computations fall within the range of the measurements up to about 240 degrees after which the radial expansion is over estimated. The LL+FW results follow the VTM behaviour in the contraction region whereas show an improvement in the expansion segment. The MB+FM results show a qualitative behaviour similar to the one observed for the previous HIGE condition. The FD+VRW predicts a too abrupt expansion at azimuth angles higher than 180 degrees.

The same considerations made for the previous HIGE condition can be repeated for the HIGE condition, at $z/R = 0.32$, shown in Fig. 6. An additional comment can however be made with reference to the BEM+FW computations which show the ¡origin of some numerical instabilities in the free wake modelling that are introduced by the extremely strong influence that the ground exerts on the rotor when it

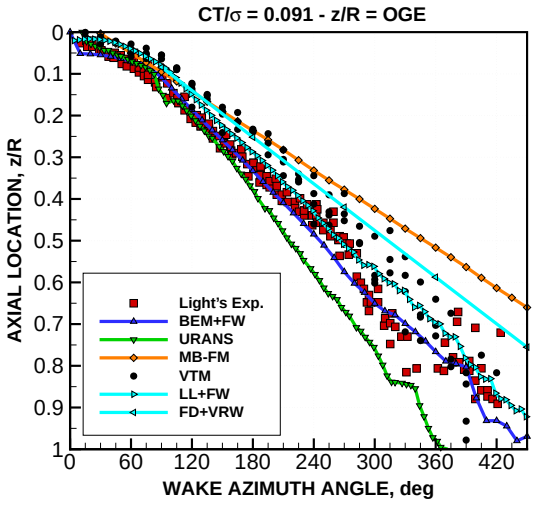


(a) Axial

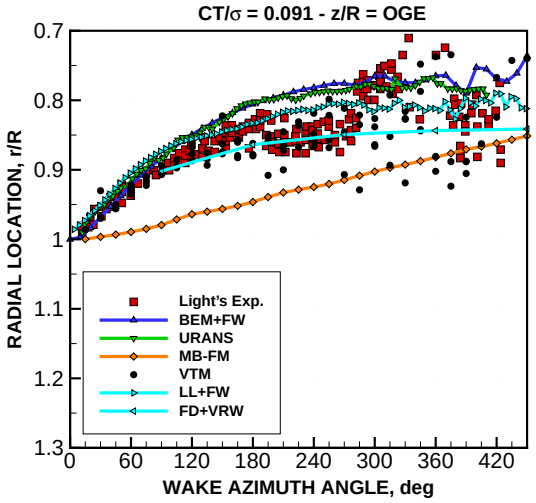


(b) Radial

Figure 2: *Tip vortex axial and radial locations; Hover out of ground effect.*

is located at such small distances from the ground. Very good agreement with test data are obtained with LL+FW especially on the radial locations of tip vortices. Finally, the MB+FM calculations refer to a $z/R = 0.36$ since instability problems have not allowed the computations at the nominal case of $z/R = 0.32$.

## 3.2 Forward Flight Experimental Data

The experimental results presented in this paper are from tests conducted on a $D = 1$m diameter,

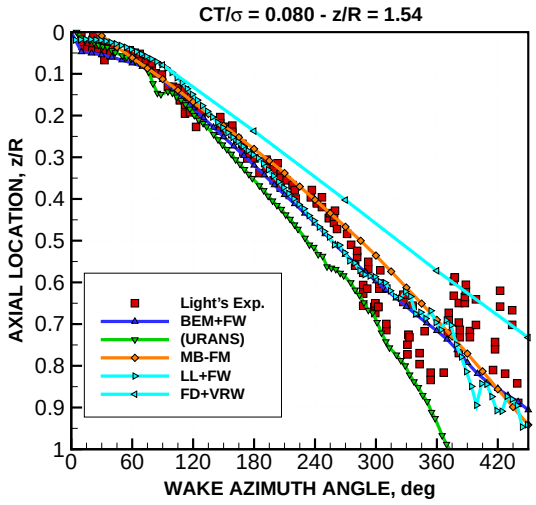


(a) Axial

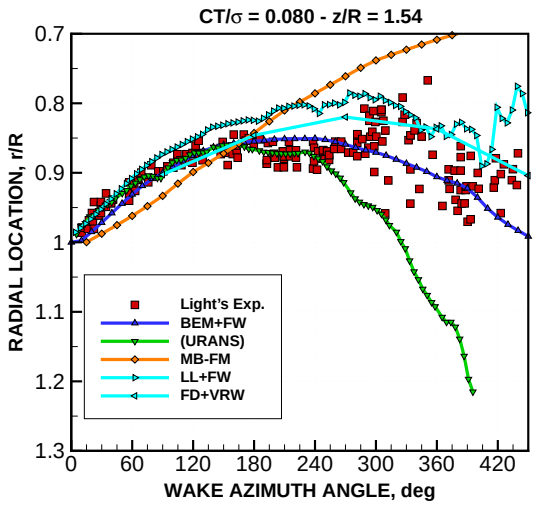


(b) Radial

Figure 3: *Tip vortex axial and radial locations; Hover in ground effect,* $z/R = 1.54$.

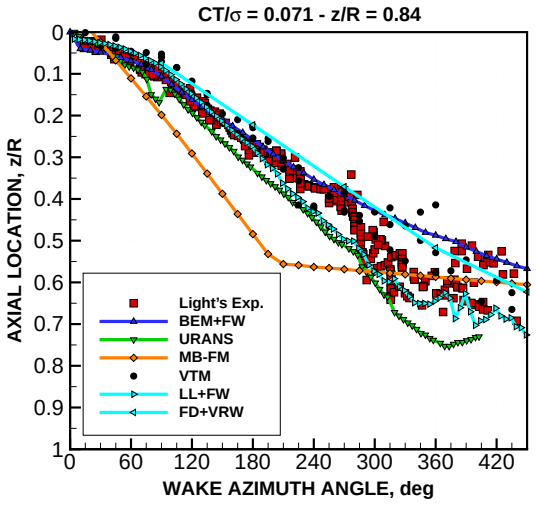


(a) Axial

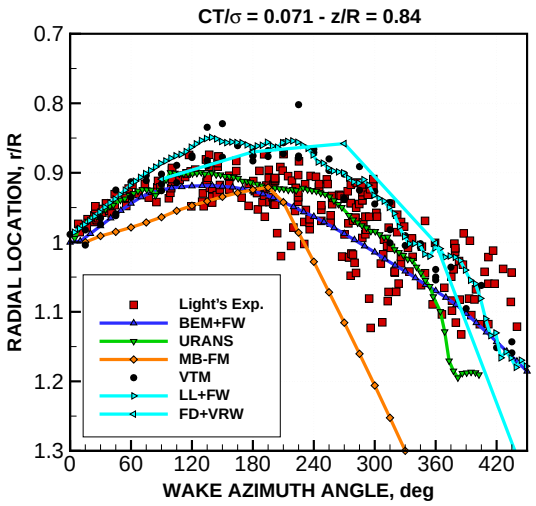


(b) Radial

Figure 4: *Tip vortex axial and radial locations; Hover in ground effect,* $z/R = 0.84$.

4-blade rotor running in a low-speed, closed-return wind tunnel with a 2.7m wide × 2.10m high × 4m long, octagonal working section. A moving ground (continuous belt moving over platen) comprised the lower surface of the working section, and Particle Image Velocimetry was used as the main experimental technique to investigate the rotor wake fluid dynamics. A schematic diagram of the experiment is shown in figure 7. The $(r, y, z)$ axis system is indicated, where $y$ is in the vertical direction, and $r$ is the radial coordinate on the rotor disk parallel to the wind tunnel longitudinal axis pointing directly upstream. All the rotor components were derived from commercially available, radio-control, scale-model parts. A feather hinge allowed for the blade collective (mean geometric angle of attack) and longitudinal and lateral cyclic pitch angles $\theta_{1s}$ and $\theta_{1c}$ to be altered, but the hub was rigid in flap and lag. The rotor was run at a speed of $n = 16$ revolutions per second. The rotor blades were untwisted, untapered and mildly cambered with a chord length of $c = 5.5$cm and thickness-to-chord ratio 12%. The rotor assembly was mounted on a load cell and sting system, and blade cyclic angles could be set such that the rotor system could be trimmed to zero rolling and pitching moment. The

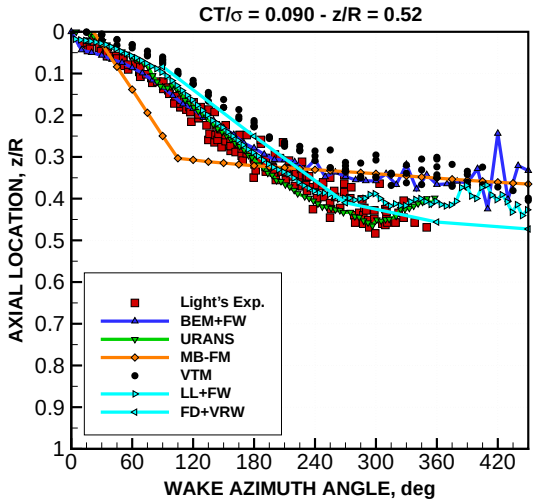


(a) Axial

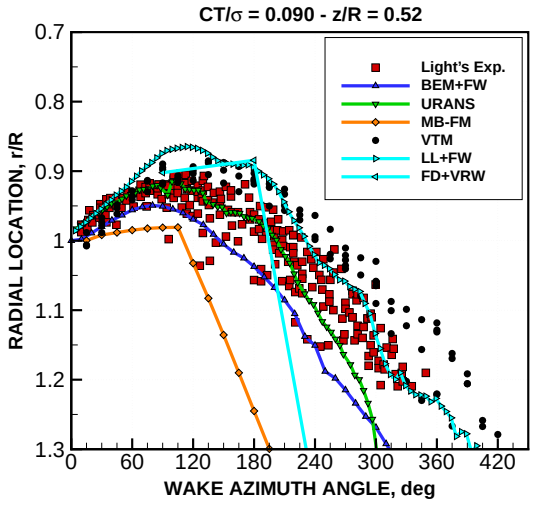


(b) Radial

Figure 5: *Tip vortex axial and radial locations; Hover in ground effect, $z/R = 0.52$.*

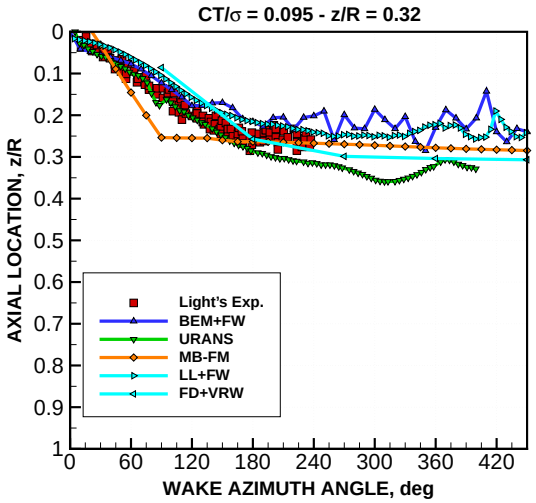


(a) Axial

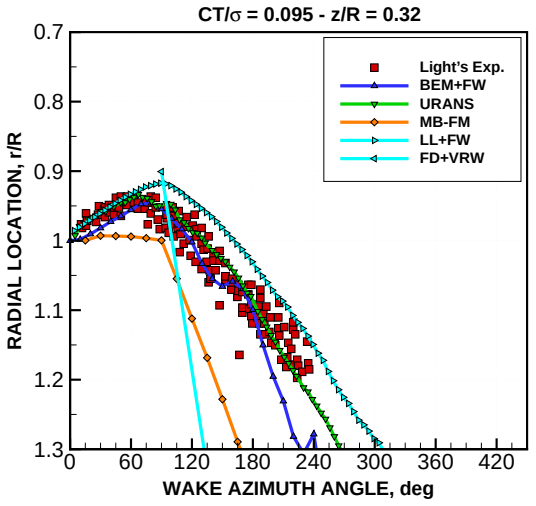


(b) Radial

Figure 6: *Tip vortex axial and radial locations; Hover in ground effect, $z/R = 0.32$.*

entire rotor assembly was mounted at the centre of the working section on the end of a long sting that allowed its height $h$ above the ground to be varied. For these tests the rotor shaft was set with no tilt and the rotor disk was in the horizontal plane. Tests were conducted with the moving ground speed set to either ground stationary relative to the rotor, $V_g = 0$, or at the same speed as the wind tunnel flow, $V_g = V_\infty$. The former condition is equivalent to the rotor stationary over the ground with the air moving past the rotor/ ground system (hover in a cross-wind), while the latter condition is representative of forward flight at speed $V_\infty$ over the ground into a still atmosphere.

A commercial system (LaVision) was used for the PIV. This was based on a dual-cavity, Nd:YAG laser, output wavelength 532nm, capable of delivering 0.5J per pulse (8ns duration), and two 14-bit, 11Mpixel digital video cameras. Each camera was fitted with 100mm or 50mm lenses ($f_\#$=2.8) mounted on Scheimpflug tilting lens mounts for sharp focus across the field of view when viewing off axis, and the system was operated using one camera

in two-component mode for the $(u, v)$ velocity field in the $(r, y)$ plane, or with both cameras in stereoscopic, three-component mode for the $(u, v, w)$ velocity field in the $(r, y)$ plane. $z-$ component vorticity $\omega$ was calculated from the $(u, v)$ velocity. The laser was expanded into a 2mm thick laser sheet, located in the vertical plane, parallel with the wind tunnel longitudinal axis and coincident with the mid-plane of the rotor disk. Due to the size of the rotor and its wake the field of view was typically around 1m (one rotor diameter) wide. A Laskin nozzle seeder was used with olive oil as the substrate, and this generated a fine oil mist with nominal particle diameter 1$\mu$m; the particle relative density and size are known to be good for PIV in air, and the only area where particle acceleration effects were apparent was in the very young trailed vortices immediately below the rotor disk. LaVision Davis 7.2 software was used for data reduction, and the measurement resolution was equivalent to one velocity measurement per 4mm square for a 1m wide field of view. Up to 120 cases were sampled per test, sufficient for an estimation of the mean flow velocity and other statistics.

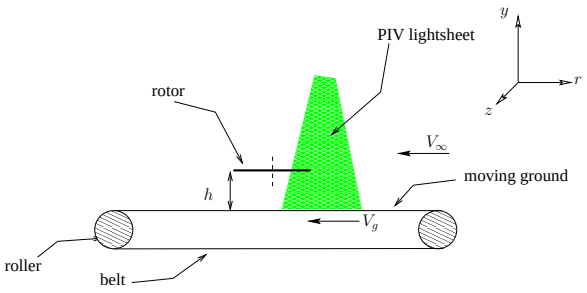


Figure 7: *Experimental setup with moving ground, PIV light sheet and sense of moving ground and wind tunnel speeds $V_g$ and $V_\infty$.*

**Test Results.** To illustrate the important effect of the moving ground on the flow and for the purposes of brevity, only sample PIV data are presented in this paper. A full set of results will be published elsewhere. Mean flow velocity from the PIV were used to derive mean flow pathlines, and these are shown in figure 8 for the trimmed rotor for frame (a) ground stationary, and frame (b) ground moving for normalised advance ratio $\mu^*$=0.76 at a rotor height of half a rotor diameter above the ground. The ground is along the $y/R = -1$ line. The salient feature in all the plots is the recirculation zone due to the ground effect, and this is shown by the clear pathline recirculation. Flow approaching the rotor lower down in the field of view and upstream of the recirculation zone passes up and around the recirculation zone, while higher up in the field of view fluid is deflected upwards and passes down through the rotor disk. The moving ground has a significant influence on the spatial extent of the ground effect recirculation zone that forms ahead of the rotor. The centre of the recirculation zone is at around $r/R = 1.3$ in the stationary ground case, and $r/R = 0.7$ in the moving ground case. The mean flow pathline topologies also show a separation point on the ground ahead of the recirculation zone, at around $r/R = 1.7$ in the stationary ground case, and $r/R = 0.9$ in the moving ground case. Figure 9 shows how the position of this topological separation point varies with normalised advance ratio and the additional effects of the rotor trim and ground speed conditions. The untrimmed rotor is with the cyclic angles set to zero, but trim only has a weak effect on the wake. On the other hand the ground velocity condition is significant, with the separation point for the ground moving case being significantly farther back compared to ground stationary. Vorticity (not presented) shows structural differences between the ground stationary and ground moving cases, and in particular the secondary separation caused by the passage of the rotor blade tip vortices along the ground is more prominent in the moving ground case. The moving ground simulates forward flight more correctly than the stationary ground, and the PIV shows that a key feature of this is the development of a boundary layer between the recirculation zone and the ground. This has clear implications for calculations of the ground effect flow field using CFD.

# 4 Conclusions

This paper has shown some problems of rotor in ground effect. Validation of several computational methods has been carried out on a specific case of hover in ground effect. The comparisons are satisfactory with most of the methods used up to a full revolution, over a range of ground clearances. However, at the lowest clearance, there is a scatter of the data, and the convergence of the computational methods becomes increasingly difficult.

Additional experimental work has been carried out to extend the database, to include the effects of the rotor flying forward. Work is ongoing to compare the various computational methods with the

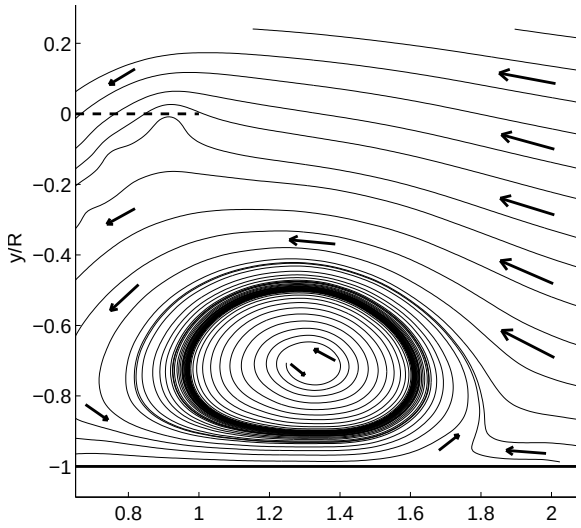


(a) $V_g/V_\infty = 0$

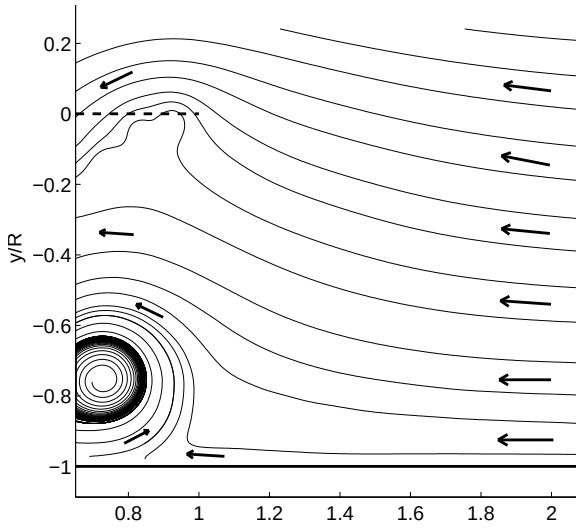


(b) $V_g/V_\infty = 1$

Figure 8: *Mean flow pathlines constructed from PIV data in the ground effect wake at $\mu^*$=0.76 for the trimmed rotor at height $h/D = 0.5$ above the ground. Horizontal and vertical axes have been scaled with rotor radius R.*

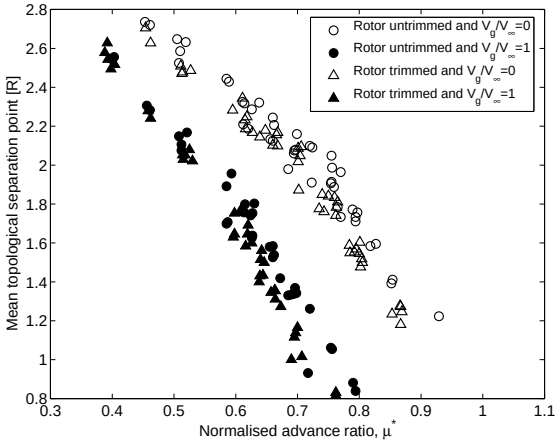


Figure 9: Effect of moving ground and trim condition on mean topological separation point over a range of normalised advance ratio for rotor at height $h/D = 0.5$ above the ground.

experiments over a range of thrust-weighted advance ratios. Work is also ongoing in related areas, such as ground effects due to inclined walls, presence of vertical ground obstacles and brownout.

## Acknowledgements

Part of this work has been carried out under the GARTEUR Helicopter Action Group HC-AG17. The authors acknowledge the contribution of Klaus-Dieter Pahlke, the monitoring responsable, and Luigi Federico (CIRA) for the support in the evaluation of CIRA's trim conditions.

# References

[1] Betz A. The ground effect on lifting propellers. Technical Report TM 836, NACA, Aug. 1927.

[2] Knight M and Hefner RA. Analysis of ground effect on the lifting airscrew. Technical Report TN-835, NACA, Dec. 1941.

[3] Cheeseman IC and Bennett WE. The effect of the ground on a helicopter rotor. R & M 3021, ARC, 1955.

[4] Hayden JS. The effect of the ground on helicopter hover power required. In *32nd AHS Annual Forum Proceedings*, Washington, DC, May 1976.

[5] Curtiss HC, Sun M, Putnam WF, and Hanker EJ. Rotor aerodynamics in ground effect at low advance ratios. *AHS Journal*, 29(1), 1984.

[6] McCauley GJ, Tsai W, and Savas Ö. An experimental study of rotorcraft in ground effect. In *Proceedings of the AHS Specialists Conference*, San Francisco, CA, Jan 2010.

[7] Filippone A and Bojdo N. Turboshaft engine air particle separation. *Prog. Aerospace Sciences*, 46:224–245, 2010.

[8] Basset PM et al. Finite state rotor induced flow model for interference and ground effect. In *57th AHS Forum*, May 2001.

[9] Basset PM and El Omari A. A rotor vortex wake model for helicopter flight mechanics and its application to the prediction of the pitch-up phenomenon. In *25th ERF Forum*, Rome, 1999.

[10] Lebouar G, Costes M, Leroy-Chesneau A, and Devinant P. Numerical simulations of unsteady aerodynamics of helicopter rotor in maneuvering flight conditions. *Aero. Science and Tech.*, 8(1):11–25, Jan 2004.

[11] Benoit B, Daquin AM, Kampa K, Grunhagen W, and Basset PM. HOST: a general helicopter tool for Germany and France. In *56th AHS Forum*, Virginia Beach, VA, May 2000.

[12] Rodriguez B. Blade vortex interaction and vortex ring state captured by a fully time marching unsteady wake model coupled with a comprehensive dynamics code. In *Heli Japan*, Saitama, Japan, Nov. 2010.

[13] Scully MP. Computation of helicopter rotor wake geometry and influence on rotor harmonic airloads. Technical Report ASRL TR 178-1, MIT, March 1975.

[14] Visingardi A, D'Alascio A, Pagano A, and Renzoni P. Validation of CIRA's rotorcraft aerodynamic modelling system with DNW experimental data. In *Proceedings of the 22nd European Rotorcraft Forum*, Brighton, UK, Sept. 1996.

[15] Ananthan S, JG Leishman, and Ramasamy M. The role of filament stretching in the free-vortex modeling of rotor wakes. In *Proceedings of the 58th AHS Forum*, Montreal, Canada, June 2002.

[16] Kroll N, Eisfeld B, and Bleeke HM. The Navier-Stokes code FLOWer. In *Notes on Numerical Fluid Mechanics*, volume 71, pages 58–71. Vieweg, 1999.

[17] Jameson A, Schmidt W, and Turkel E. Numerical solutions of the euler equations by finite volume methods using runge-kutta time-stepping schemes. AIAA Paper 1981-1259, 1981.

[18] Jameson A. Time dependent calculations using multigrid, with applications to unsteady flows past airfoils and wings. AIAA Paper 1991-1596.

[19] Wilcox DC. Reassessment of the scale-determining equation for advanced turbulence models. *AIAA J.*, 26(11), Nov. 1988.

[20] Brown RE. Rotor wake modeling for flight dynamic simulations of helicopters. *AIAA J.*, 38(1), Jan 2000.

[21] Brown RE and Line AJ. Efficient high-resolution wake modeling using the vorticity transport equation. *AIAA J.*, 43(7), July 2005.

[22] Phillips C and Brown RE. Eulerian simulation of the fluids dynamics of helicopter brownout. *J. Aircraft*, 46(4), July 2009.

[23] Light JS. Tip vortex geometry of a hovering helicopter rotor in ground effect. In *45th AHS Annual Forum*, Boston, MA, May 1989.

[24] Kutz B, Bensing F, Ke$\beta$ler M, and Krämer E. CFD calculation of a helicopter rotor hovering in ground effect. In *STAB Meeting*, Berlin, 2010.